

# Cetuximab–Polymersome–Mertansine Nanodrug for Potent and Targeted Therapy of EGFR-Positive Cancers

Shujing Yue, Yifan Zhang, Yaohua Wei, Rainer Haag, Huanli Sun,\* and Zhiyuan Zhong\*



Cite This: *Biomacromolecules* 2022, 23, 100–111



Read Online

ACCESS |



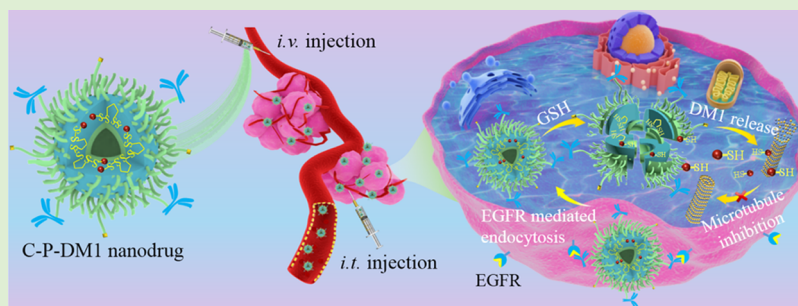
Metrics & More



Article Recommendations



Supporting Information



**ABSTRACT:** Targeted nanomedicines particularly armed with monoclonal antibodies are considered to be the most promising advanced chemotherapy for malignant cancers; however, their development is hindered by their instability and drug leakage problems. Herein, we constructed a robust cetuximab–polymersome–mertansine nanodrug (C-P-DM1) for highly potent and targeted therapy of epidermal growth factor receptor (EGFR)-positive solid tumors. C-P-DM1 with a tailored cetuximab surface density of 2 per P-DM1 exhibited a size of ca. 60 nm, high stability with minimum DM1 leakage, glutathione-triggered release of native DM1, and 6.0–11.3-fold stronger cytotoxicity in EGFR-positive human breast (MDA-MB-231), lung (A549), and liver (SMMC-7721) cancer cells ( $IC_{50} = 27.1–135.5$  nM) than P-DM1 control. Notably, intravenous injection of C-P-DM1 effectively repressed subcutaneous MDA-MB-231 breast cancer and orthotopic A549-Luc lung carcinoma in mice without inducing toxic effects. Strikingly, intratumoral injection of C-P-DM1 completely cured 60% of mice bearing breast tumor without recurrence. This robust cetuximab–polymersome–mertansine nanodrug provides a promising new strategy for targeted treatment of EGFR-positive solid malignancies.

## 1. INTRODUCTION

Therapeutic monoclonal antibodies with high specificity have recently experienced an unprecedented development for cancer therapy, wherein over 30 products entered the market with large sales.<sup>1–4</sup> Among them, the epidermal growth factor receptor (EGFR), which is amplified 20- to 50-fold in multiple tumors and which stimulated the tumor growth and progression, represents one important oncological target.<sup>5–8</sup> To date, four anti-EGFR antibodies have been marketed in combination with chemotherapy or as a monotherapy to treat EGFR-positive cancers.<sup>9,10</sup> To mitigate chemotherapeutics-related systemic toxicity and drug resistance, antibody-drug conjugates (ADCs) that can surmount the disadvantages of both nonspecific chemotherapeutics and specific but often inefficient antibodies have gained increasing interest for tumor-specific drug delivery.<sup>11–14</sup> For instance, several anti-EGFR ADCs using potent cytotoxic drugs (e.g., mertansine, DM1) or photosensitizer IRDye 700DX as payloads are under clinical evaluations in patients with EGFR-positive solid tumors including triple negative breast cancer (TNBC) and nonsmall cell lung cancer (NSCLC).<sup>15–18</sup> Although significant antitumor efficacy is observed, low drug content remain a primary

challenge for ADCs, causing large antibody consumption and high cost.<sup>19–21</sup>

Ligand-installed nanomedicines are reported as an effective tactic to improve drug loading and realize effective tumor-targeted drug delivery.<sup>22–26</sup> In the past decades, a range of EGFR-targeted nanotherapies were engineered *via* tethering the GE11 peptide, anti-EGFR antibody, and fragment,<sup>27–30</sup> among which anti-EGFR antibody and fragment-decorated immunonanosystems have attracted much attention due to their high specificity and affinity. For example, cetuximab (FDA approved)-modified poly(lactic-*co*-glycolic acid) (PLGA) nanoparticles and liposomes have been developed for EGFR-targeted delivery of conventional chemotherapeutics including taxanes, doxorubicin (DOX), camptothecin, and so forth.<sup>31–34</sup> There-

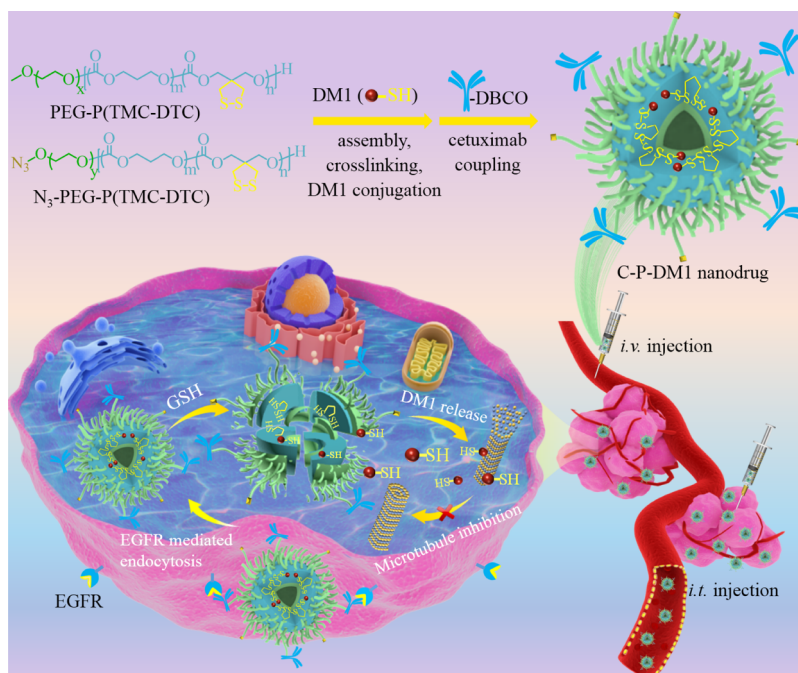
Received: August 16, 2021

Revised: December 6, 2021

Published: December 16, 2021



**Scheme 1. Schematic Showing the Fabrication of Cetuximab–Polymersome–DM1 Nanodrug (C-P-DM1) for EGFR-Targeted Delivery of DM1 to Potently Treat EGFR-Positive Solid Malignancies *via* Intravenous (*i.v.*) or Intratumoral (*i.t.*) Injection**



into, cetuximab fragment-coupled immunoliposomes encapsulating DOX with good antitumor performance have been promoted to phase II clinical trials for solid tumors.<sup>35</sup> Nevertheless, these immuno-nanosystems were hindered by the instability and drug leakage problems, leading to compromised therapeutic effects. The post-antibody modification needed for most immuno-nanosystems brings forward high requests for nanocarriers, which should not only be robust by itself but also stably load drugs to prevent drug leakage during preparation.

Herein, we developed a robust cetuximab–polymersome–DM1 nanodrug (C-P-DM1) with high drug to antibody ratio (DAR), minimum DM1 leakage, and glutathione (GSH)-triggered DM1 release for highly potent and targeted therapy of EGFR-positive solid tumors *in vivo* (Scheme 1). The polymersomes based on poly(ethylene glycol)-*b*-poly(trimethylene carbonate-*co*-dithiolane trimethylene carbonate) [PEG-P-(TMC-DTC)] have shown a high stability owing to disulfide crosslinking of the membrane.<sup>36,37</sup> DM1 can be facilely and covalently conjugated to the polymersomal membrane *via* disulfide linkage.<sup>38,39</sup> Notably, by incorporating azide-functionalized PEG-P(TMC-DTC) into the polymersomes, cetuximab can be engineered at their surface *via* click chemistry. C-P-DM1 represents an innovative EGFR-specific nanotoxin that elegantly combines the advantages of ADCs and nanomedicines for treating TNBC and NSCLC tumors.

## 2. EXPERIMENTAL SECTION

**2.1. Materials and Characterizations.** The details on materials and characterizations utilized in this paper are listed in the Supporting Information.

**2.2. Preparation of Azide-functionalized Polymersomes (N<sub>3</sub>-P) and Polymersome–Mertansine Nanodrug (N<sub>3</sub>-P-DM1).** N<sub>3</sub>-P was fabricated *via* the co-assembly of N<sub>3</sub>-PEG-P(TMC-DTC) and PEG-P(TMC-DTC) with a molar ratio of 1.8:98.2 (2:98 w/w) accompanied by simultaneous self-crosslinking of the polymersomal membrane. Here, PEG-P(TMC-DTC) ( $M_n = 5.0$ –(14.8–2.0) kDa,

$M_w/M_n = 1.1$ ) and N<sub>3</sub>-PEG-P(TMC-DTC) with a longer PEG chain ( $M_n = 7.9$ –(15.0–2.0) kDa,  $M_w/M_n = 1.1$ ) were synthesized similarly to our previous reports.<sup>40–42</sup> The resulting N<sub>3</sub>-P had an  $M_w$  of  $1.54 \times 10^7$  Da, equivalent to *ca.* 637 polymer chains in each polymersome.<sup>38</sup> By facilely adding DM1 in the course of assembly, N<sub>3</sub>-P-DM1 with covalently conjugated DM1 *via* disulfide linkages can be conveniently prepared in a relatively large scale. In brief, 2.23 mL of DM1 solution (10 mg/mL) in *N,N*-dimethylformamide (DMF) was added into 93 mL of phosphate buffer (PB, 10 mM, pH 7.4) and stirred at 37 °C, followed by continuous injection of 200 mg of polymers dissolved in 5 mL of DMF. After overnight incubation at 37 °C, the dispersion was dialyzed (Spectra/Pore, MWCO: 3.5 kDa) against PB for 8 h to remove DMF, followed by extensive purification using a tangential flow filtration system (MWCO: 10 kDa) with PB containing 20% ethanol (v/v) and PB as the medium sequentially. Thus, the obtained N<sub>3</sub>-P-DM1 was concentrated to 18 mg/mL, filtrated under the sterile condition, and stored in a 4 °C refrigerator. Size distribution of N<sub>3</sub>-P-DM1 and its stability during long-term storage were monitored *via* dynamic light scattering (DLS). The content of DM1 was determined *via* high-performance liquid chromatography (HPLC) equipped with a C18 column (ChromCore 120, 5  $\mu$ m, 4.6  $\times$  250 mm) at a wavelength of 252 nm using the mixture of water and acetonitrile (v/v = 40/60) as the mobile phase. Drug conjugation content (DCC) and efficiency (DCE) were therefore calculated based on the following formula

$$\text{DCC (wt \%)} = \frac{\text{weight of conjugated DM1}}{\text{total weight of conjugated DM1 and polymers}} \times 100$$

$$\text{DCE (\%)} = \frac{\text{weight of conjugated DM1}}{\text{weight of DM1 in feed}} \times 100$$

To confirm the covalent conjugation of DM1 rather than physical loading in polymersomes, N<sub>3</sub>-P-DM1 was incubated with acetonitrile and measured by HPLC. DM1 leakage from N<sub>3</sub>-P-DM1 during long-term storage was monitored similarly.

Cy5-labeled polymersomes (N<sub>3</sub>-P-Cy5) were prepared similarly *via* co-assembly of PEG-P(TMC-DTC)-Cy5, N<sub>3</sub>-PEG-P(TMC-DTC), and PEG-P(TMC-DTC) at a molar ratio of 20.4:2.2:77.4.

**2.3. Preparation of Cetuximab–Polymersome–Mertansine Nanodrug (C-P-DM1).** C-P-DM1 was fabricated *via* post-decoration of N<sub>3</sub>-P-DM1 with cetuximab through strain-promoted click reaction. First, cetuximab was functionalized with dibenzocyclooctyne (DBCO) by adding 13.5  $\mu$ L of NHS-PEG<sub>4</sub>-DBCO (5 mg/mL) in DMSO into 500  $\mu$ L of cetuximab (10 mg/mL) in PBS with subsequent overnight reaction at room temperature (r.t.). Cetuximab–DBCO was then collected *via* carrying out ultrafiltration thrice (MWCO: 10 kDa) using PBS. Its concentration was measured *via* HPLC installed with a BioCore SEC-300 column (5  $\mu$ m, 7.8  $\times$  300 mm). To determine the DBCO functionality, cetuximab–DBCO and native cetuximab were measured by matrix-assisted laser desorption ionization time-of-flight mass spectrometry (MALDI-TOF-MS) at a cetuximab concentration of  $\sim$ 1.0 mg/mL.

Freshly prepared cetuximab–DBCO (6 mg/mL in PBS) was mixed with N<sub>3</sub>-P-DM1 or N<sub>3</sub>-P-Cy5 (18 mg/mL) at N<sub>3</sub> to cetuximab–DBCO molar ratios of 1:0.25, 1:0.5, 1:1, and 1:2, respectively, for overnight reaction in a shaker (100 rpm, 25  $^{\circ}$ C). Afterward, unreacted cetuximab–DBCO was removed and collected by thrice ultrafiltration (MWCO: 300 kDa) using PBS, yielding C-P-DM1 or C-P-Cy5 with different cetuximab surface densities. By quantifying the unreacted cetuximab–DBCO *via* HPLC, the weight of conjugated cetuximab could be calculated. The number of cetuximab per P-DM1 nanodrug could be further calculated based on the following equation.

$$\text{Number of cetuximab per nanodrug} = \frac{\text{weight of conjugated cetuximab}}{\text{molecular weight of cetuximab}} \times \frac{M_w \text{ of } N_3 - P}{\text{weight of } N_3 - P}$$

Size distribution of C-P-DM1 and its stability against 10–100-fold dilution with PBS or in the presence of 10% fetal bovine serum (FBS) were measured by DLS. Blank cetuximab–polymersomes (C-P) were prepared similarly *via* clicking cetuximab–DBCO onto N<sub>3</sub>-P. The secondary structure of cetuximab prior to and after conjugation onto the polymersome surface was detected using the circular dichroism (CD) spectrum.

Reduction-triggered DM1 release from C-P-DM1 was evaluated *via* dialysis against 10 mM GSH in PB (10 mM, pH 7.4) or PB only ( $n = 3$ ). Briefly, 0.5 mL of C-P-DM1 in each dialysis tube (MWCO: 14 kDa) was dialyzed against 20 mL of different media at 37  $^{\circ}$ C and 200 rpm. 5 mL of release medium was sampled at different time points (0.5, 1, 2, 4, 6, 8, 10, 12, and 24 h), followed by lyophilization and redissolution in 0.3 mL of acetonitrile for HPLC measurements. Fresh release medium (5 mL) was supplemented after each sampling.

**2.4. EGFR Expression Levels on the Surface of Cancer Cells.** MDA-MB-231 TNBC cells, A549 NSCLC cells, SMMC-7721 hepatocellular carcinoma cells, and L929 fibroblast cells ( $5 \times 10^5$  cells) were suspended in 100  $\mu$ L of PBS containing 1% bovine serum albumin (BSA) and incubated with 5  $\mu$ L of PE anti-human EGFR antibody (Biolegend) for 40 min. Cells were then collected by centrifugation, washed three times using PBS, resuspended in PBS (500  $\mu$ L), and immediately analyzed by a FACS Calibur flow cytometer (Beckton Dickinson, U.S.A.). For each sample,  $10^4$  cells were analyzed at least, and FlowJo\_10 software was used to process the data. The details on cell culture are shown in the [Supporting Information](#).

**2.5. Cellular Uptake Studies.** Cellular uptake and targetability of C-P-DM1 in EGFR-positive cancer cells were studied using C-P-Cy5 with different cetuximab surface densities *via* flow cytometry. EGFR-negative L929 fibroblast cells were used as a control. MDA-MB-231 ( $5 \times 10^5$  cells/well), A549, SMMC-7721, or L929 cells ( $3 \times 10^5$  cells/well) seeded in six-well plates were incubated with C-P-Cy5 or P-Cy5 (40 ng Cy5 equiv/mL) at 37  $^{\circ}$ C for 4 h. Cells were then detached using trypsin, centrifuged at 1000 rpm for 3 min, washed twice with PBS, and resuspended in 500  $\mu$ L of PBS. Fluorescence histograms of over  $1 \times 10^4$  cells were immediately recorded using PBS-treated cells as a control.

To study the uptake mechanism of C-P-Cy5 and P-Cy5, MDA-MB-231 cells were precultured 1 h with different endocytic inhibitors, including methyl- $\beta$ -cyclodextrins (M $\beta$ CD, 1 mg/mL), amiloride hydrochloride (1 mg/mL), chlorpromazine (CPZ, 10  $\mu$ g/mL), and dynasore (80  $\mu$ M) under 37  $^{\circ}$ C. Then, C<sub>2</sub>-P-Cy5 or P-Cy5 (40 ng Cy5

equiv/mL) was added for 1 h incubation, followed by a treatment similar to that mentioned above for flow cytometry analysis. Cells directly treated with C<sub>2</sub>-P-Cy5 or P-Cy5 were used as controls.

Confocal laser scanning microscopy (CLSM) was then utilized to visualize the cellular uptake of C-P-Cy5. MDA-MB-231 ( $8 \times 10^4$  cells/well), A549, or SMMC-7721 cells ( $3 \times 10^4$  cells/well) cultured in 24-well plates with preplaced glass slides were incubated with C<sub>2</sub>-P-Cy5 or P-Cy5 (1.7  $\mu$ g Cy5 equiv/mL) at 37  $^{\circ}$ C for 4 h. Cells were then washed thrice with PBS and fixed by 4% paraformaldehyde (PFA) in PBS for 15 min. Cytoskeleton and cell nuclei were stained with tetramethylrhodamine (TRITC)-labeled phalloidin for 50 min and 4',6-diamidino-2-phenylindole (DAPI) for 3 min, respectively, using PBS washing after each staining. Finally, stained cells adhered on glass slides were put onto microslides to take fluorescence images using CLSM (Leica TCS SPS).

To investigate the intracellular trafficking of C-P-Cy5, MDA-MB-231 cells ( $8 \times 10^4$  cells/well) were incubated with C<sub>2</sub>-P-Cy5 (6  $\mu$ g Cy5 equiv/mL) at 37  $^{\circ}$ C for 2 and 4 h, respectively. Endo/lysosomes were then stained using LysoTracker Green (200 nM) at 37  $^{\circ}$ C for 1 h, with subsequent PFA fixing and DAPI staining to take CLSM images.

**2.6. In Vitro Cytotoxicity and Tubulin Polymerization Inhibition of C-P-DM1.** The cytotoxicity of C-P-DM1 with different cetuximab densities, P-DM1, and free DM1 against EGFR-positive MDA-MB-231, A549, and SMMC-7721 cells was evaluated by 3-(4,5-dimethylthiazol-2-yl)-2,5-diphenyltetrazolium bromide (MTT) assays. EGFR-negative L929 cells were used as a control. Cells seeded in 96-well plates (MDA-MB-231 and L929: 3000 cells/well, A549 and SMMC-7721: 2000 cells/well) were incubated with 20  $\mu$ L of different DM1 formulations in PBS for 4 h at 37  $^{\circ}$ C. Here, final DM1 concentrations were set at 0.001–13.5  $\mu$ M. Afterward, medium was replaced into fresh ones for another 68 h incubation, followed by the addition of 10  $\mu$ L of MTT solution (5 mg/mL in PBS) into each well. After 4 h incubation at 37  $^{\circ}$ C, medium was carefully removed and 150  $\mu$ L of DMSO was added into each well to dissolve the generated formazan, thus measuring its absorbance at 570 nm *via* a microplate reader. The absorbance of cells following treatment with different DM1 formulations was compared to that of PBS-treated cells to calculate the cell viability (%). The cytotoxicity of native cetuximab (0.67–66.7 nM) and blank polymersomes (C-P and N<sub>3</sub>-P, 4–120  $\mu$ g/mL) was investigated under a similar procedure using MDA-MB-231 cells.

The capability of C-P-DM1 in tubulin polymerization inhibition was studied by immunocytochemistry. Typically, MDA-MB-231 cells ( $8 \times 10^4$  cells/well) seeded in 24-well plates with preplaced glass slides were incubated with C-P-DM1, P-DM1, or free DM1 for 4 h at a DM1 concentration of 541.7 nM, followed by thrice wash with PBS and fixing with 4% PFA in PBS for 15 min. After permeabilizing cells with 0.1% Triton X-100 for 5 min and blocking with 5% BSA, tubulin was immunostained with rat anti-human  $\beta_3$  tubulin monoclonal antibody (Santa Cruz) for 1.5 h and further incubated with Alexa Flour 647-labeled anti-rat IgG (Molecular Probes) for 1 h at r.t. Cell nuclei were counterstained with DAPI for 3 min, followed by through wash with PBS. Cells adhered on glass slides were mounted on microscope slides for CLSM measurements.

DM1-induced tubulin polymerization inhibition is known to cause cell cycle arrest in the G<sub>2</sub>/M phase of cancer cells. We hence evaluated cell cycle arrest of MDA-MB-231 cells after incubation with free DM1, P-DM1, or C-P-DM1. In brief, cells seeded in 6-well plates ( $3 \times 10^5$  cells/well) were incubated with different formulations at a DM1 concentration of 541.7 nM for 4 h, followed by additional 20 h incubation in fresh medium. After trypsinization, cells were washed and redispersed in cold PBS (1 mL) with the subsequent addition of 4 mL of ethanol (95%, v/v) on ice for 24 h incubation at 4  $^{\circ}$ C. Cells were then collected by centrifugation (1000 rpm, 3 min), stained with propidium iodide solution containing RNase A for 30 min in the dark prior to flow cytometry measurements (488 nm). The percentage of cells in different cycles was analyzed using FlowJo\_10 software.

**2.7. Mouse Model Establishment, Fluorescence Imaging, and Biodistribution.** Mice were handled under protocols approved by the Soochow University Laboratory Animal Center and the Animal Care and Use Committee of Soochow University. To evaluate the *in vivo* targetability and antitumor efficacy of C-P-DM1, a small piece of

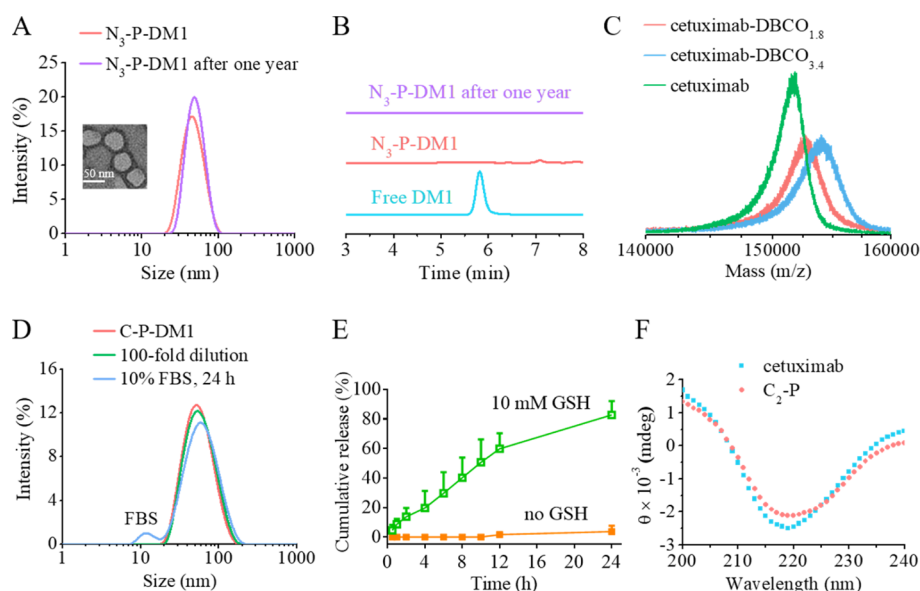


**Figure 1.** Characterization of  $N_3$ -P-DM1 and C-P-DM1 nanodrugs. (A) Size distribution of freshly prepared  $N_3$ -P-DM1 and that after 1 year storage at 4 °C. The inset shows the transmission electron microscopy image of  $N_3$ -P-DM1. (B) HPLC curves of  $N_3$ -P-DM1 and that after 1 year storage at 4 °C, using free DM1 as a control. (C) MALDI-TOF-MS analysis of cetuximab and cetuximab-DBCO. (D) Stability of C-P-DM1 against 100-fold dilution to a final polymersome concentration of 10  $\mu\text{g/mL}$  or adding 10% FBS. (E) *In vitro* DM1 release curves of C-P-DM1 in the presence or absence of 10 mM GSH. (F) Secondary structure of cetuximab prior to and after conjugation on the polymersome surface, as detected *via* CD.

MDA-MB-231 carcinoma was inoculated into the right flank of 6-week old BALB/c nude mice to establish the subcutaneous MDA-MB-231 TNBC model. The orthotopic A549-Luc human NSCLC model was established by injecting  $1 \times 10^7$  A549-Luc cells in 50  $\mu\text{L}$  of PBS containing 30% matrigel gel into the lung of each nude mice (BALB/c, 6 weeks). When MDA-MB-231 tumors reached *ca.* 300–400  $\text{mm}^3$ , 200  $\mu\text{L}$  of C-P-Cy5 or P-Cy5 in PBS (0.02  $\mu\text{g}$  Cy5/mouse) was administrated *via* tail vein injection ( $n = 3$ ). Fluorescence images of tumor-bearing mice were acquired at 1, 2, 4, 6, 8, 12, and 24 h post *i.v.* injection using a near-infrared fluorescence imaging system (Caliper IVIS Lumina II).

*Ex vivo* imaging and DM1 distribution studies were further performed to evaluate the targetability of C-P-Cy5/DM1. MDA-MB-231 tumor bearing mice were randomly grouped to receive 200  $\mu\text{L}$  of C-P-Cy5/DM1 or P-Cy5/DM1 *via* tail vein injection ( $n = 3$ ). DM1 and Cy5 dosages were set at 0.4 mg/kg and 0.02  $\mu\text{g}$ /mouse, respectively. At 6 h after injection, tumors and normal organs were collected to take fluorescence images and determine the DM1 content *via* LC-MS/MS installed with an AQ C18 column (5  $\mu\text{m}$ ,  $2.1 \times 50$  mm). For LC-MS/MS measurements, each tissue was homogenized in methanol (0.95 mL) using a homogenizer (IKA T25), followed by overnight incubation with 20 mM DTT at 37 °C. Afterward, the supernatant of each homogenate was collected by centrifugation at 6000 rpm for 10 min and then filtered with a 0.22  $\mu\text{m}$  membrane for analysis. Here, the  $m/z$  transition of DM1 from 738.3 to 541.7 was monitored to determine its content. The mobile phase was the mixture of 0.1% formic acid (FA) in  $\text{H}_2\text{O}$  and 0.02% FA in MeOH ( $v/v = 60/40$ ) with a flow rate of 0.4 mL/min.

**2.8. *In Vivo* anti-TNBC Effect of C-P-DM1 by Systemic and Local Administration.** Anti-tumor experiments of C-P-DM1 in subcutaneous MDA-MB-231 TNBC-bearing mice were initiated when average tumor volumes reached about 150  $\text{mm}^3$  (defined as day 0) *via* both *i.v.* and *i.t.* administration ( $n = 5$ ). For systemically administrated groups, mice were injected with PBS, P-DM1, or C-P-DM1 *via* tail vein at 0.4 mg DM1 equiv/kg every 4 days for a total of four times. Here, PBS-treated mice were shared with our another work.<sup>38</sup> Tumor length ( $L$ ) and width ( $W$ ) were measured every 2 days using calipers to calculate the tumor volumes ( $V = 0.5 \times L \times W^2$ ). Body weights of mice were recorded every 2 days and compared to their initial data on day 0. On day 16, blood was collected randomly from three mice in each group for blood routine analysis. On day 28 after treatment, one mouse was

randomly sacrificed from each group to isolate major organs and tumor for histological analysis *via* hematoxylin and eosin (H&E) and TUNEL staining.

For locally administrated groups, C-P-DM1 in 50  $\mu\text{L}$  of PBS was intratumorally injected on day 0 and 4 with 0.2 and 0.4 mg DM1 equiv/kg, respectively. The mice were monitored in a manner similar to that mentioned above to observe the changes of tumor volumes and body weight, as well as the histology of major organs and tumors.

**2.9. *In Vivo* anti-NSCLC Effect of C-P-DM1.** *In vivo* anti-NSCLC efficacy of C-P-DM1 was evaluated in orthotopic A549-Luc human NSCLC-bearing mice. Tumor growth was followed using an IVIS Lumina imaging system, and bioluminescence images were taken at 10 min after intraperitoneal injection of D-luciferin (75  $\mu\text{L}$ , 15 mg/mL in PBS) under isoflurane anesthesia. When the bioluminescence intensity of tumor-bearing mice reached  $1\text{--}4 \times 10^7$  p/s (defined as day 0), the mice were divided into three groups ( $n = 6$ ) and injected with C-P-DM1, P-DM1, or PBS *via* tail vein at 0.4 mg DM1 equiv/kg every 4 days for a total of four times. For each group, three mice were used to visualize the tumor growth by bioluminescence imaging. Bioluminescence imaging and weight of mice in different groups were monitored every 4 days. On day 24 post treatment, one mouse from each group was randomly sacrificed to isolate organs for histological analysis.

**2.10. Statistical Analysis.** All data were presented as mean  $\pm$  standard deviation. Statistical differences of three or more groups were evaluated *via* one-way ANOVA. When the result was significant, Tukey's post hoc test was employed for further pairwise comparisons.  $*p < 0.05$ ,  $**p < 0.01$ ,  $***p < 0.001$ .

### 3. RESULTS AND DISCUSSION

**3.1. Fabrication and Characterization of Cetuximab-Polymersome-Mertansine Nanodrug (C-P-DM1).** C-P-DM1 was conveniently fabricated *via* post-coupling reaction of cetuximab with azide groups on the surface of  $N_3$ -P-DM1. Here,  $N_3$ -P-DM1 incorporating 6 wt % conjugated DM1 (DCE: 60%) was prepared from the assembly of PEG-P(TMC-DTC) with 2 wt % of  $N_3$ -PEG-P(TMC-DTC) having a longer PEG chain (7.9 vs 5.0 kg/mol), accompanied by simultaneous self-crosslinking of the polymersomal membrane *via* ring-opening polymer-

ization of dithiolane and DM1 conjugation through thiol-disulfide exchange reaction. N<sub>3</sub>-P-DM1 with an average size of 53.2 nm and polydispersity index (PDI) of 0.15 displayed a typical vesicular structure and was robust during 1 year storage in the fridge, not merely maintaining a similar size and also no DM1 leakage (Figure 1A,B). This robust polymersome–DM1 nanodrug with the simple fabrication procedure and stable drug conjugation offers a great possibility to enable cell-specific drug delivery by post-antibody modification, outperforming polymer prodrug nanoparticles with complex design and multistep synthesis.<sup>43,44</sup>

In order to click cetuximab onto N<sub>3</sub>-P-DM1, cetuximab was first functionalized with DBCO by reaction with NHS-PEG<sub>4</sub>-DBCO at molar ratios of 1:3 and 1:6, forming cetuximab–DBCO<sub>1.8/3.4</sub> with 1.8 and 3.4 DBCO groups per cetuximab on average, respectively, as determined by MALDI-TOF-MS (Figure 1C). Cetuximab–DBCO<sub>1.8</sub> was hereafter employed to prepare C-P-DM1 *via* overnight reaction with N<sub>3</sub>-P-DM1. By varying the molar ratios of cetuximab–DBCO<sub>1.8</sub> to N<sub>3</sub> from 0.25:1, 0.5:1, and 1:1 to 2:1, C<sub>x</sub>-P-DM1 was obtained with adjustable cetuximab densities (*x*) of 1, 2, 5, and 8 cetuximab per P-DM1, respectively. C-P-DM1 exhibited a gradual increase in sizes from 58.5 to 66.4 nm with an increase of cetuximab density from 1 to 8 yet all with similar size distribution (PDI: 0.21–0.25) (Table 1). Notably, no DM1 leakage was observed during

**Table 1. Characterization of C-P-DM1 Prepared from N<sub>3</sub>-P-DM1 with a DCC of 6 wt % and DCE of 60%**

P-DM1 nanodrugs	cetuximab/N <sub>3</sub> (mol/mol)	number of cetuximab per nanodrug <sup>a</sup>	size (nm) <sup>b</sup>	PDI <sup>b</sup>
N <sub>3</sub> -P-DM1			53.2	0.15
C <sub>1</sub> -P-DM1	0.25:1	1.0 ± 0.5	58.5	0.23
C <sub>2</sub> -P-DM1	0.5:1	2.0 ± 0.5	60.1	0.22
C <sub>5</sub> -P-DM1	1:1	5.0 ± 1.0	62.5	0.25
C <sub>8</sub> -P-DM1	2:1	8.0 ± 2.0	63.2	0.21

<sup>a</sup>Measured by HPLC. <sup>b</sup>Determined by DLS.

the post-conjugation of cetuximab–DBCO<sub>1.8</sub> and the obtained C-P-DM1 had high stability against either 10–100-fold dilution or incubation in 10% FBS, showing negligible DM1 release in PB (10 mM, pH 7.4) (Figures S1, 1D,E). Nevertheless, 80% of DM1 was released from C-P-DM1 in 24 h once treating with 10 mM GSH (Figure 1E). Importantly, CD spectra exhibited that cetuximab decorated on the surface of polymersomes maintained a similar secondary structure to native cetuximab (Figure 1F). It is worth noting that C-P-DM1 had a high DAR of 152–1220, which was 1–2 orders of magnitude higher than that of ADCs (DAR: 3–8).<sup>45,46</sup> For instance, T-DM1, an ADC used clinically for treating HER2-positive breast cancers, has a DAR of 3.5.<sup>47</sup> The high DAR of C-P-DM1 significantly reduces the use of antibodies, which may not only lowers the costs but also lessens complications related to high dose of antibodies.

**3.2. In Vitro Cellular Uptake and Antitumor Efficacy of C-P-DM1.** EGFR, as one important oncological target, has been employed for targeted treatment of diverse solid tumors.<sup>48–50</sup> EGFR levels on the surface of MDA-MB-231, A549, SMMC-7721, and L929 cells were examined using PE anti-human EGFR antibody and measured *via* flow cytometry. It is shown that EGFR is overexpressed on the membrane of MDA-MB-231, A549, and SMMC-7721 cancer cells, in line with previous studies,<sup>51–55</sup> while expressed at a low level on normal L929

fibroblast cells (Figure 2A). These cells were subsequently utilized for cellular uptake and cytotoxicity studies to validate the EGFR targetability of C-P-DM1.

First, Cy5-labeled polymersomes (C-P-Cy5 and P-Cy5) were utilized for visualizing their cellular uptake by flow cytometry. Regardless of cetuximab densities, C-P-Cy5 all exhibited significantly augmented cellular uptake in EGFR-positive MDA-MB-231, SMMC-7721, and A549 cancer cells compared to nontargeted P-Cy5. C<sub>2</sub>-P-Cy5 with the best targetability in MDA-MB-231 and SMMC-7721 cells displayed 10.5- and 35.8-fold higher internalization, respectively, and 18.2-fold higher cellular uptake in A549 cells as well (Figure 2B), largely surpassing GE11 peptide-modified nanosystems.<sup>56,57</sup> However, in EGFR-negative L929 fibroblast cells, negligible cellular uptake was observed for both C<sub>2</sub>-P-Cy5 and P-Cy5 (Figure 2B). Figure 2C shows that the internalization of C<sub>2</sub>-P-Cy5 in MDA-MB-231 cells was significantly repressed by CPZ, dynasore, amiloride hydrochloride, as well as MβCD, signifying that receptor-mediated endocytosis, macropinocytosis, and caveolae-dependent endocytosis all contributed to its uptake. However, the internalization of P-Cy5 was mainly mediated by dynamin, macropinocytosis, and caveolae-dependent pathways (Figure 2D).

Furthermore, much stronger Cy5 fluorescence in C<sub>2</sub>-P-Cy5-treated MDA-MB-231, SMMC-7721, and A549 cells than P-Cy5-treated ones was detected by CLSM (Figure 2E), confirming the EGFR-targetability and boosted cellular internalization of C-P-Cy5 in EGFR-positive cancer cells. Endo/lysosome trafficking images showed that C-P-Cy5 was located primarily in the cell membrane and endo/lysosomes of MDA-MB-231 cells after 2 h incubation and then gradually distributed to the cytosol, supporting its effective cellular uptake *via* the endo/lysosome trafficking pathway (Figure S2).

Consistent with the flow cytometry analysis, C-P-DM1 with 1, 2, 5, and 8 cetuximab on each nanodrug all showed extraordinary potency over P-DM1 in inhibiting the growth of EGFR-positive cancer cells (Figure 3A–C). Thereinto, C<sub>2</sub>-P-DM1 was most potent in MDA-MB-231 and SMMC-7721 cells, displaying half-maximal inhibitory concentration (IC<sub>50</sub>) values of *ca.* 33.8 and 27.1 nM, respectively, 6.0- and 11.3-fold lower than that of P-DM1 (Figure 3A,B). In EGFR-positive A549 cells, C<sub>2</sub>-P-DM1, C<sub>5</sub>-P-DM1, and C<sub>8</sub>-P-DM1 induced comparable toxicity with an IC<sub>50</sub> of 135.5 nM, decreasing by 6.6-fold in comparison to P-DM1 (Figure 3C). In sharp contrast, for EGFR-negative L929 cells, C-P-DM1 with different cetuximab densities caused cytotoxicity similar to P-DM1 with an IC<sub>50</sub> of about 333.3 nM (Figure 3D), which was over 10-fold greater than C<sub>2</sub>-P-DM1 in EGFR-positive MDA-MB-231 and SMMC-7721 cells. It is evident that C-P-DM1 can selectively target EGFR-positive cancer cells with high affinity and strong cytotoxicity. Hereafter, C<sub>2</sub>-P-DM1 was utilized for further studies and called C-P-DM1. Importantly, blank polymersomes (C-P and Ps) and native cetuximab were practically nontoxic toward MDA-MB-231 cells at a polymersome and cetuximab concentration as high as 120 and 66.7 nM, respectively (Figure 3E,F), which is in line with previous reports.<sup>58,59</sup> It is known that cetuximab reduces receptor activation and the associated downstream signaling by preventing the binding of endogenous ligands as well as stimulating EGFR internalization and degradation, thus exerting its antitumor effects.<sup>60</sup> A high amount of cetuximab is generally required to inhibit the proliferation of cancer cells (*e.g.*, over 667 nM for MDA-MB-231 cells).<sup>61</sup> Herein, C-P-DM1 using cetuximab as a targeting ligand can achieve specific EGFR-

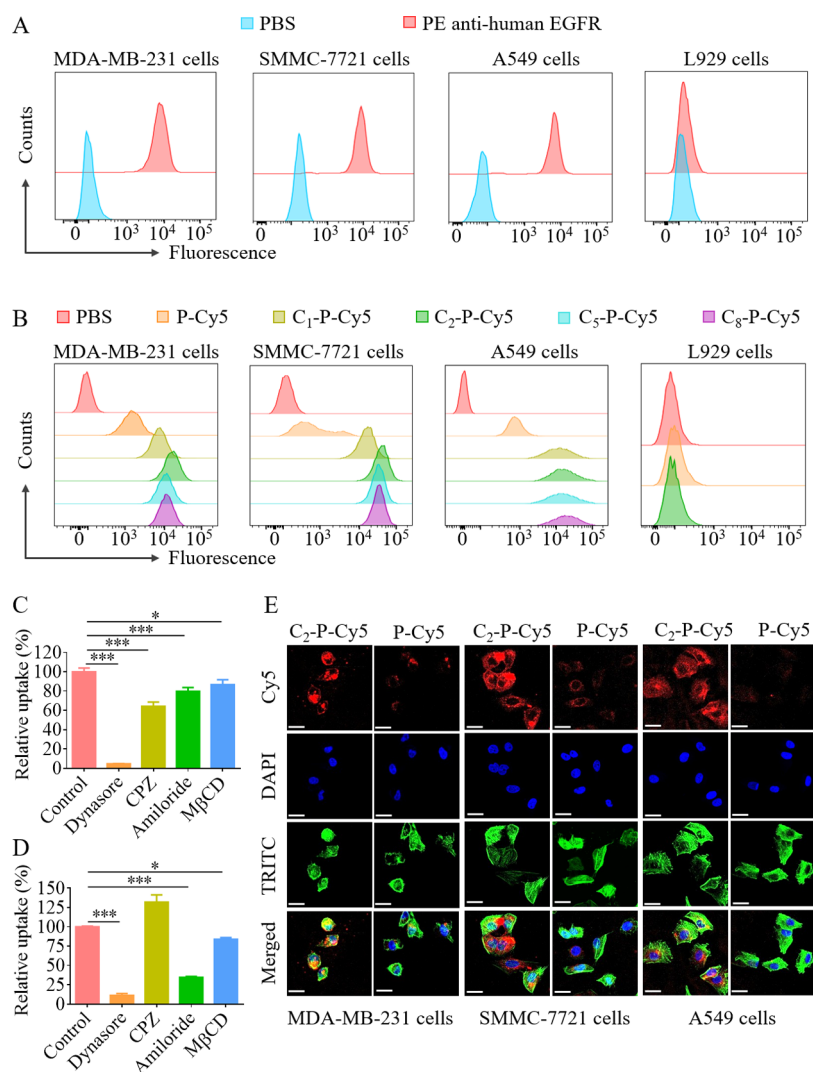


**Figure 2.** Cellular uptake and targetability of C-P-Cy5 in EGFR-positive cancer cells. (A) Flow cytometry analysis of EGFR expression levels of different cells using PE anti-human EGFR antibody. (B) Flow cytometry analysis of MDA-MB-231, SMMC-7721, A549, and L929 cells following 4 h incubation with C<sub>2</sub>-P-Cy5 or P-Cy5. Cellular uptake of (C) C<sub>2</sub>-P-Cy5 and (D) P-Cy5 in MDA-MB-231 cells preincubated with diverse endocytic inhibitors ( $n = 3$ ). \* $p < 0.05$ , \*\*\* $p < 0.001$ . (E) CLSM images of EGFR-positive cancer cells following 4 h treatment with C<sub>2</sub>-P-Cy5 or P-Cy5; scale bars are 25  $\mu\text{m}$ . Cy5 (red) for polymersomes, DAPI (blue) for cell nuclei, and TRITC-stained cytoskeleton was pseudo-colored in green.

targeted delivery of DM1 to EGFR-positive cancer cells, inducing potent toxicity with a cetuximab concentration as low as 73 pM.

It is reported that DM1 can interfere with microtubule formation, thereby causing cell cycle arrest and apoptosis.<sup>62–64</sup> As expected, C-P-DM1 more effectively destabilized the microtubules in MDA-MB-231 cells than P-DM1, as shown by immunofluorescent staining (Figure 3G). Consequently, C-P-DM1 treatment at a DM1 concentration of 541.7 nM dramatically increased G2/M phase arrest of MDA-MB-231 cells from 20.5% (PBS control) to 94.3%, which was higher than P-DM1 (73.7%) and free DM1 (82.8%) (Figure 3H). It is obvious from these results that C-P-DM1 can selectively target EGFR-positive cancer cells with high affinity, efficient cellular uptake, and fast DM1 release inside cells, inducing effective microtubule destabilization, cell cycle arrest, and potent antitumor activity.

### 3.3. Biodistribution and Antitumor Effect of C-P-DM1.

To investigate the *in vivo* targetability and antitumor performance of C-P-DM1 in EGFR-positive tumors, subcutaneous

MDA-MB-231 TNBC and orthotopic A549-Luc NSCLC xenograft in nude mice were established. *In vivo* fluorescence images revealed that C-P-Cy5 quickly accumulated in the tumor site after intravenous administration into subcutaneous MDA-MB-231 TNBC-bearing mice, showing constantly stronger tumoral Cy5 fluorescence than P-Cy5 over the whole imaging period from 1 to 24 h (Figure 4A). Maximum tumor enrichment of C-P-Cy5 was observed at 6 h post injection, which was 5.2-fold higher compared to nontargeted P-Cy5 (Figure 4B). *Ex vivo* fluorescence images at 6 h post injection further revealed that C-P-Cy5/DM1 had significantly more tumor accumulation than P-Cy5/DM1, while no obvious enhancement in major organs (Figure 4C). Consistently, DM1 content in tumors of mice-receiving C-P-Cy5/DM1 was 4.7-fold higher than that of P-Cy5/DM1, but comparable in major organs as determined by LC-MS/MS (Figure 4D). The markedly improved tumor accumulation of C-P-DM1 over P-DM1 is likely due to its high stability with minimum drug leakage and optimal antibody density. Of note, cetuximab-decorated vitamin E D- $\alpha$ -tocopheryl polyethylene glycol succinate (TPGS) micelles and anti-EGFR-

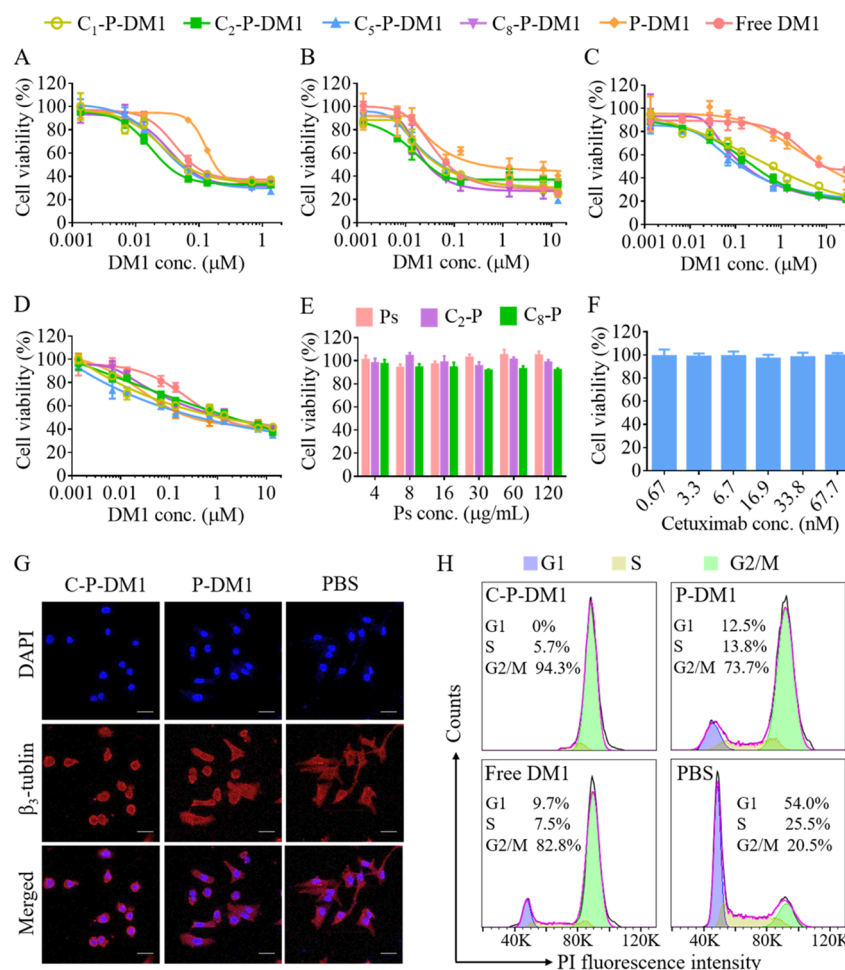


**Figure 3.** Cytotoxicity, tubulin inhibition, and cell cycle arrest analysis. Cytotoxicity of C-P-DM1 and P-DM1 in (A) MDA-MB-231, (B) SMMC-7721, (C) A549, and (D) L929 cells. Cytotoxicity of (E) C-P and Ps as well as (F) free cetuximab in MDA-MB-231 cells ( $n = 4$ ). (G) Immunofluorescence images of the microtubule structure in MDA-MB-231 cells following incubation with C-P-DM1, P-DM1, or PBS (DM1: 541.7 nM). Scale bars: 50  $\mu\text{m}$ . (H) Cell cycle analysis of MDA-MB-231 cells after incubation with C-P-DM1, P-DM1, free DM1, or PBS for 4 h and fresh medium for additional 20 h.

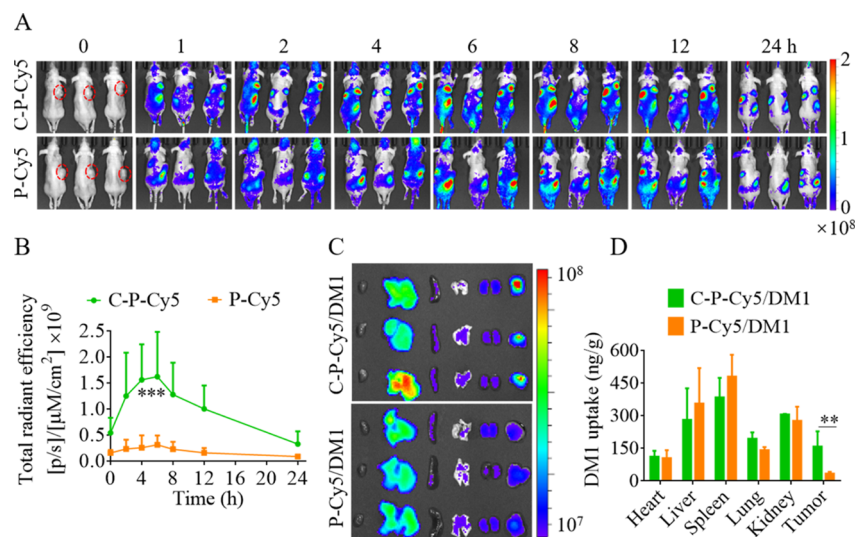


**Figure 4.** Fluorescence images and biodistribution of subcutaneous MDA-MB-231 tumor-bearing mice following tail vein injection of C-P-Cy5/DM1 or C-P-Cy5/DM1 ( $n = 3$ ). (A) Time-lapsed *in vivo* fluorescence images and (B) semiquantitative fluorescence analysis in the tumor site. *Ex vivo* fluorescence images and (D) DM1 distribution in tumors and major organs at 6 h post injection.  $**p < 0.01$ ,  $***p < 0.001$ .

modified PEG–PLGA micellar DOX were reported with only 2–3-fold enhancement in tumor accumulation than their

nontargeted control in subcutaneous MDA-MB-231 or MDA-MB-468 TNBC-bearing mice.<sup>34,65</sup>

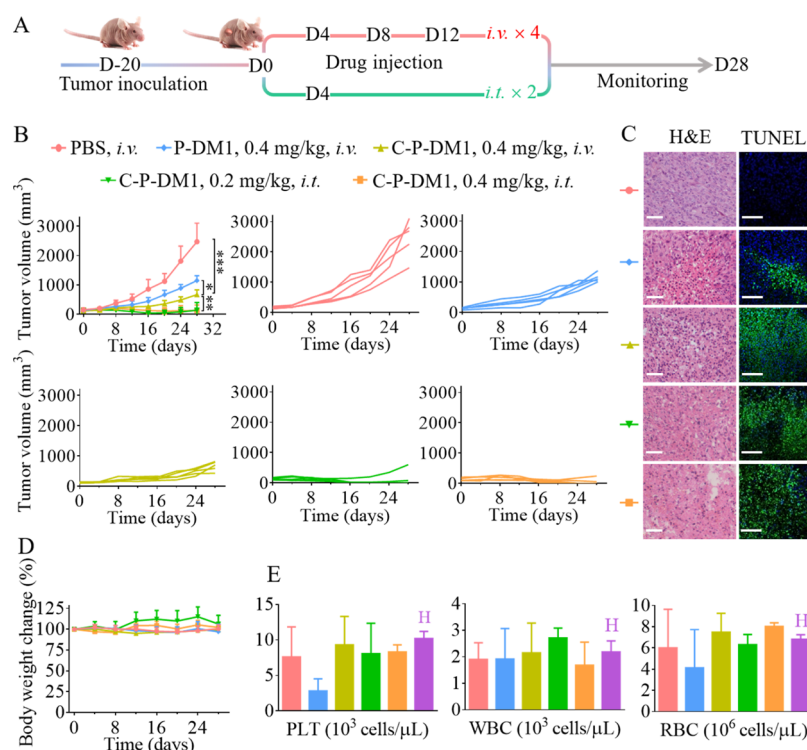


**Figure 5.** Therapeutic effect of C-P-DM1 and P-DM1 in subcutaneous MDA-MB-231 TNBC-bearing mice. (A) Schematic diagram of the TNBC model establishment, therapy, and monitoring schedule. (B) Tumor volume changes after different treatments ( $n = 5$ ).  $*p < 0.05$ ,  $**p < 0.01$  and  $***p < 0.001$ . (C) H&E- and TUNEL-stained images of tumor tissues isolated on day 28. Scale bars are 50  $\mu\text{m}$ . (D) Body weight changes of mice in different groups. (E) Blood routine analysis of mice after 4 days of the last administration ( $n = 3$ , H: healthy mice).

Anti-TNBC studies of C-P-DM1 in the subcutaneous MDA-MB-231 TNBC model were performed by *i.v.* or *i.t.* injection and started on day 0, when tumor volume reached an average of 150  $\text{mm}^3$  (Figure 5A). Four times *i.v.* administration of C-P-DM1 at an interval of 4 days significantly inhibited tumor growth, showing much smaller tumor size compared to P-DM1- ( $*p < 0.05$ ) and PBS ( $***p < 0.001$ )-treated groups (Figure 5B). We have previously studied the antitumor efficacy of free DM1 in diverse tumor models including subcutaneous MDA-MB-231 TNBC, wherein only a slight tumor inhibition effect was observed at 0.4 mg/kg or even higher dosages.<sup>39,66–68</sup> Intriguingly, *i.t.* injection of C-P-DM1 at the same dosage or a lower one (0.2 mg DM1 equiv/kg) on day 0 and 4 both cured 60% of mice without recurrence, exhibiting a tumor inhibition rate of 94.5%. Moreover, C-P-DM1 treatment whether by *i.v.* or *i.t.* administration induced apparent cell shrinkage, incomplete cell membrane, and TUNEL-positive apoptosis of tumor cells, which were noticeably more compared to the P-DM1 group (Figure 5C). Importantly, negligible damage to major organs and no obvious change in body weight were observed for mice with different treatments (Supporting Information Figures S3 and 5D), and supporting C-P-DM1 and P-DM1 nanodrugs were well tolerated. In the meantime, mice following treatment with C-P-DM1 (*i.v.* or *i.t.*) maintained blood routine parameters including platelet (PLT), white blood cell (WBC), and red blood cell (RBC) in the normal range and comparable to PBS and healthy controls (Figure 5E). However, PLT and RBC levels of P-DM1-treated mice were slightly decreased.

To further validate the EGFR-targeted antitumor efficacy of C-P-DM1, anti-NSCLC studies in orthotopic human A549-Luc NSCLC-bearing mice were further performed *via i.v.* injection and initiated when tumor luminescence intensity increased to

$1-4 \times 10^7$  p/s (denoted as day 0) (Figure 6A). After four dose administration of C-P-DM1 at 0.4 mg DM1 equiv/kg, mice with orthotopic A549-Luc NSCLC exhibited obvious tumor growth suppression, maintaining a relatively low bioluminescence level throughout the imaging period from day 0 to day 24 (Figure 6B,C). The proliferation of A549-Luc cells in P-DM1-treated mice was inhibited to a certain degree during the administration, but quickly recovered from day 8, inducing 4.2-fold higher tumor burden than C-P-DM1. However, mice in the PBS group showed a continuous and sharp luminescence increase by 47-fold to day 24 and suffered body weight loss, consequently leading to rapid death (Figure 6B–E). Compared to PBS, median survival was prolonged by 20 days in the group of C-P-DM1 (Figure 6E). The photographs of lungs isolated on day 24 displayed aggressive tumor growth and invasion to the lung lobes of PBS- or P-DM1-treated mice, and C-P-DM1 was clearly most potent in tumor inhibition (Figure 6F). H&E images of lung slices further showed that C-P-DM1-treated mice had negligible tumor invasion and normal alveolar. In sharp contrast, significant tumor infiltration was observed in mice treated with PBS or P-DM1, causing alveolar damage and deformation (Figure 6G). Importantly, mice in different groups all maintained their weight during administration and no obvious damage was observed in major organs (Supporting Information Figure S4). It is evident from these results that C-P-DM1 can mediate safe and targeted delivery of DM1 to EGFR-positive solid tumors, potentially inhibiting tumor growth.

#### 4. CONCLUSIONS

In conclusion, we have developed a robust polymersome–mertansine nanodrug (P-DM1) with zero drug leakage, making it convenient for post-modification of cetuximab to obtain an

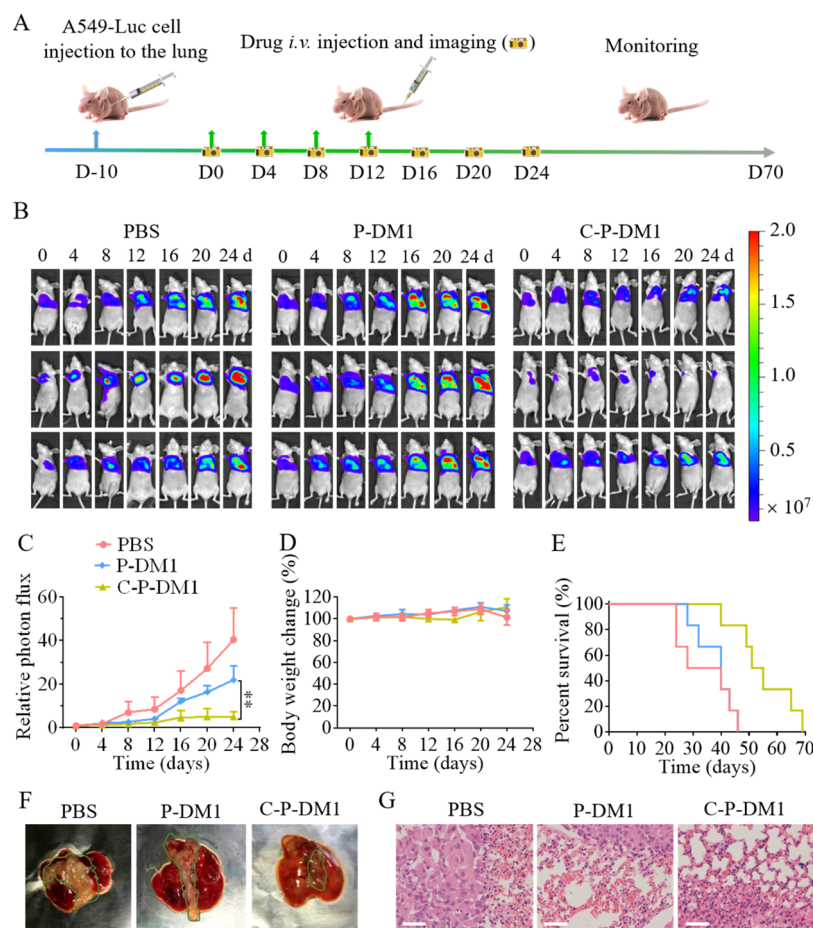


**Figure 6.** Therapeutic efficacy of C-P-DM1 in orthotopic A549-Luc NSCLC-bearing mice. P-DM1 and PBS were employed as controls. (A) Establishment, therapy, and monitoring scheme of the orthotopic A549-Luc NSCLC model. (B) Bioluminescence imaging and (C) quantitative bioluminescence levels of mice from day 0 to day 24 ( $n = 3$ ). (D) Body weight change and (E) Kaplan–Meier survival curves of mice ( $n = 6$ , C-P-DM1 vs P-DM1 and PBS, \*\* $p < 0.01$ ). (F) Photographs and (G) H&E stained images of lung isolated from different groups on day 24. Scale bars are 50  $\mu\text{m}$ .

EGFR-selective C-P-DM1 nanodrug for advanced therapy of EGFR-positive tumors. The resulting C-P-DM1 with stable DM1 conjugation can elegantly overcome the instability and drug leakage problems encountered in most immuno-nano-systems, realizing specific and effective delivery of highly potent toxins. Systemic injection of C-P-DM1 effectively repress subcutaneous breast tumor and orthotopic lung carcinoma in mice, without inducing toxic effects. Of note, intratumoral injection of C-P-DM1 completely cures 60% of mice with breast tumor. This robust C-P-DM1 nanodrug provides a new and promising strategy for targeted treatment of EGFR-positive solid malignancies.

## ASSOCIATED CONTENT

### Supporting Information

The Supporting Information is available free of charge at <https://pubs.acs.org/doi/10.1021/acs.biomac.1c01065>.

Details on materials, characterization and cell culture; stability of C-P-DM1 against dilution; endo/lysosome trafficking of C-P-Cy5 in MDA-MB-231 cells, and H&E stained images of major organs (PDF)

## AUTHOR INFORMATION

### Corresponding Authors

**Huanli Sun** – Biomedical Polymers Laboratory, Jiangsu Key Laboratory of Advanced Functional Polymer Design and Application, College of Chemistry, Chemical Engineering and Materials Science, and State Key Laboratory of Radiation Medicine and Protection, Soochow University, Suzhou 215123, P. R. China; [orcid.org/0000-0001-6287-1555](https://orcid.org/0000-0001-6287-1555); Phone: +86-512-65880098; Email: [sunhuanli@suda.edu.cn](mailto:sunhuanli@suda.edu.cn); Fax: +86-512-65880098

**Zhiyuan Zhong** – Biomedical Polymers Laboratory, Jiangsu Key Laboratory of Advanced Functional Polymer Design and Application, College of Chemistry, Chemical Engineering and Materials Science, and State Key Laboratory of Radiation Medicine and Protection, Soochow University, Suzhou 215123, P. R. China; [orcid.org/0000-0003-4175-4741](https://orcid.org/0000-0003-4175-4741); Email: [zyzhong@suda.edu.cn](mailto:zyzhong@suda.edu.cn)

### Authors

**Shujing Yue** – Biomedical Polymers Laboratory, Jiangsu Key Laboratory of Advanced Functional Polymer Design and Application, College of Chemistry, Chemical Engineering and Materials Science, and State Key Laboratory of Radiation Medicine and Protection, Soochow University, Suzhou 215123, P. R. China

**Yifan Zhang** – Biomedical Polymers Laboratory, Jiangsu Key Laboratory of Advanced Functional Polymer Design and Application, College of Chemistry, Chemical Engineering and Materials Science, and State Key Laboratory of Radiation Medicine and Protection, Soochow University, Suzhou 215123, P. R. China

**Yaohua Wei** – Biomedical Polymers Laboratory, Jiangsu Key Laboratory of Advanced Functional Polymer Design and Application, College of Chemistry, Chemical Engineering and Materials Science, and State Key Laboratory of Radiation Medicine and Protection, Soochow University, Suzhou 215123, P. R. China

**Rainer Haag** – Department of Biology, Chemistry and Pharmacy, Institute for Chemistry and Biochemistry, Freie Universität Berlin, Berlin 14195, Germany

Complete contact information is available at:

<https://pubs.acs.org/10.1021/acs.biomac.1c01065>

### Author Contributions

S.Y. and Y.Z. contributed equally to this work. The manuscript was written through contributions of all authors. All authors have given approval to the final version of the manuscript.

### Notes

The authors declare no competing financial interest.

## ACKNOWLEDGMENTS

This work was supported by the National Natural Science Foundation of China (51633005, 52073196, and 51761135117), the Natural Science Foundation of the Jiangsu Higher Education Institutions of China (21KJA150007), and the Deutsche Forschungsgemeinschaft (DFG).

## REFERENCES

- (1) Rajewsky, K. The advent and rise of monoclonal antibodies. *Nature* **2019**, *575*, 47–49.
- (2) Sliwkowski, M. X.; Mellman, I. Antibody therapeutics in cancer. *Science* **2013**, *341*, 1192–1198.
- (3) Scott, A. M.; Wolchok, J. D.; Old, L. J. Antibody therapy of cancer. *Nat. Rev. Cancer* **2012**, *12*, 278–287.
- (4) Yasunaga, M. Antibody therapeutics and immunoregulation in cancer and autoimmune disease. *Semin. Cancer Biol.* **2020**, *64*, 1–12.
- (5) Sigismund, S.; Avanzato, D.; Lanzetti, L. Emerging functions of the EGFR in cancer. *Mol. Oncol.* **2018**, *12*, 3–20.
- (6) Guardiola, S.; Varese, M.; Sánchez-Navarro, M.; Giral, E. A third shot at EGFR: New opportunities in cancer therapy. *Trends Pharmacol. Sci.* **2019**, *40*, 941–955.
- (7) Chong, C. R.; Jänne, P. A. The quest to overcome resistance to EGFR-targeted therapies in cancer. *Nat. Med.* **2013**, *19*, 1389–1400.
- (8) Uribe, M. L.; Marrocco, I.; Yarden, Y. EGFR in cancer: Signaling mechanisms, drugs, and acquired resistance. *Cancers* **2021**, *13*, 2748.
- (9) Xu, M. J.; Johnson, D. E.; Grandis, J. R. EGFR-targeted therapies in the post-genomic era. *Cancer Metastasis Rev.* **2017**, *36*, 463–473.
- (10) Agustoni, F.; Suda, K.; Yu, H.; Ren, S.; Rivard, C. J.; Ellison, K.; Caldwell, C.; Rozeboom, L.; Brovsky, K.; Hirsch, F. R. EGFR-directed monoclonal antibodies in combination with chemotherapy for treatment of non-small-cell lung cancer: An updated review of clinical trials and new perspectives in biomarkers analysis. *Cancer Treat. Rev.* **2019**, *72*, 15–27.
- (11) Beck, A.; Goetsch, L.; Dumontet, C.; Corvaia, N. Strategies and challenges for the next generation of antibody-drug conjugates. *Nat. Rev. Drug Discovery* **2017**, *16*, 315–337.
- (12) Chau, C. H.; Steeg, P. S.; Figg, W. D. Antibody-drug conjugates for cancer. *Lancet* **2019**, *394*, 793–804.
- (13) Drago, J. Z.; Modi, S.; Chandralapaty, S. Unlocking the potential of antibody-drug conjugates for cancer therapy. *Nat. Rev. Clin. Oncol.* **2021**, *18*, 327–344.
- (14) Coats, S.; Williams, M.; Kebble, B.; Dixit, R.; Tseng, L.; Yao, N.-S.; Tice, D. A.; Soria, J.-C. Antibody-drug conjugates: Future directions in clinical and translational strategies to improve the therapeutic index. *Clin. Cancer Res.* **2019**, *25*, S441–S448.
- (15) Goss, G. D.; Vokes, E. E.; Gordon, M. S.; Gandhi, L.; Papadopoulos, K. P.; Rasco, D. W.; Fischer, J. S.; Chu, K. L.; Ames, W. W.; Mittapalli, R. K.; Lee, H.-J.; Zeng, J.; Roberts-Rapp, L. A.; Loberg, L. I.; Ansell, P. J.; Reilly, E. B.; Ocampo, C. J.; Holen, K. D.; Tolcher, A. W. Efficacy and safety results of depatuxizumab mafodotin (ABT-414) in patients with advanced solid tumors likely to overexpress epidermal growth factor receptor. *Cancer* **2018**, *124*, 2174–2183.
- (16) Xu, R.-h.; Qiu, M.-Z.; Zhang, Y.; Wei, X.-L.; Hu, C. First-in-human dose-escalation study of anti-EGFR ADC MRG003 in patients with relapsed/refractory solid tumors. *J. Clin. Oncol.* **2020**, *38*, 3550.
- (17) Lakhani, N.; Chandana, S.; Tolcher, A.; Cole, Y.; Rivas, K.; Sinclair, S.; Nadler, P. I.; Wood, D. L.; Papadopoulos, K. P. A phase Ia/Ia trial of AVID100, an anti-EGFR antibody-drug conjugate. *Cancer Res.* **2019**, *79*, CT056.
- (18) Cognetti, D. M.; Johnson, J. M.; Curry, J. M.; Mott, F.; Kochuparambil, S. T.; McDonald, D.; Fidler, M. J.; Stenson, K.; Vasani, N. R.; Razaq, M.; Campana, J. P.; Biel, M. A.; Gillenwater, A. M. Results of a phase 2a, multicenter, open-label, study of RM-1929 photo-immunotherapy (PIT) in patients with locoregional, recurrent head and neck squamous cell carcinoma (rHNSCC). *J. Clin. Oncol.* **2019**, *37*, 6014.
- (19) Yurkovetskiy, A. V.; Yin, M.; Bodyak, N.; Stevenson, C. A.; Thomas, J. D.; Hammond, C. E.; Qin, L.; Zhu, B.; Gumerov, D. R.; Ter-Ovanesyan, E.; Uttard, A.; Lowinger, T. B. A polymer-based antibody-vinca drug conjugate platform: Characterization and preclinical efficacy. *Cancer Res.* **2015**, *75*, 3365–3372.
- (20) Dan, N.; Setua, S.; Kashyap, V.; Khan, S.; Jaggi, M.; Yallapu, M.; Chauhan, S. Antibody-drug conjugates for cancer therapy: Chemistry to clinical implications. *Pharmaceuticals* **2018**, *11*, 32.
- (21) Lyon, R. P.; Bovee, T. D.; Doronina, S. O.; Burke, P. J.; Hunter, J. H.; Neff-LaFord, H. D.; Jonas, M.; Anderson, M. E.; Setter, J. R.; Senter, P. D. Reducing hydrophobicity of homogeneous antibody-drug conjugates improves pharmacokinetics and therapeutic index. *Nat. Biotechnol.* **2015**, *33*, 733–735.
- (22) Alibakhshi, A.; Abarghooi Kahaki, F.; Ahangarzadeh, S.; Yaghoobi, H.; Yarian, F.; Arezumand, R.; Ranjbari, J.; Mokhtarzadeh, A.; de la Guardia, M. Targeted cancer therapy through antibody fragments-decorated nanomedicines. *J. Controlled Release* **2017**, *268*, 323–334.
- (23) Hu, X. L.; Kwon, N.; Yan, K. C.; Sedgwick, A. C.; Chen, G. R.; He, X. P.; James, T. D.; Yoon, J. Bio-Conjugated Advanced Materials for Targeted Disease Theranostics. *Adv. Funct. Mater.* **2020**, *30*, 1907906.
- (24) Mi, P.; Cabral, H.; Kataoka, K. Ligand-Installed Nanocarriers toward Precision Therapy. *Adv. Mater.* **2020**, *32*, 1902604.
- (25) Sun, H.; Dong, Y.; Feijen, J.; Zhong, Z. Peptide-decorated polymeric nanomedicines for precision cancer therapy. *J. Controlled Release* **2018**, *290*, 11–27.
- (26) Gu, W.; Meng, F.; Haag, R.; Zhong, Z. Actively targeted nanomedicines for precision cancer therapy: Concept, construction, challenges and clinical translation. *J. Controlled Release* **2021**, *329*, 676–695.
- (27) Li, C.; Cai, G.; Song, D.; Gao, R.; Teng, P.; Zhou, L.; Ji, Q.; Sui, H.; Cai, J.; Li, Q.; Wang, Y. Development of EGFR-targeted evodiamine nanoparticles for the treatment of colorectal cancer. *Biomater. Sci.* **2019**, *7*, 3627–3639.
- (28) Jin, H.; Pi, J.; Zhao, Y.; Jiang, J.; Li, T.; Zeng, X.; Yang, P.; Evans, C. E.; Cai, J. EGFR-targeting PLGA-PEG nanoparticles as a curcumin delivery system for breast cancer therapy. *Nanoscale* **2017**, *9*, 16365–16374.
- (29) Nguyen, P. V.; Allard-Vannier, E.; Chourpa, I.; Hervé-Aubert, K. Nanomedicines functionalized with anti-EGFR ligands for active

targeting in cancer therapy: Biological strategy, design and quality control. *Int. J. Pharm.* **2021**, *605*, 120795.

(30) Mondal, G.; Kumar, V.; Shukla, S. K.; Singh, P. K.; Mahato, R. I. EGFR-targeted polymeric mixed micelles carrying gemcitabine for treating pancreatic cancer. *Biomacromolecules* **2016**, *17*, 301–313.

(31) McDaid, W. J.; Greene, M. K.; Johnston, M. C.; Pollheimer, E.; Smyth, P.; McLaughlin, K.; Van Schaeuybroeck, S.; Straubinger, R. M.; Longley, D. B.; Scott, C. J. Repurposing of cetuximab in antibody-directed chemotherapy-loaded nanoparticles in EGFR therapy-resistant pancreatic tumours. *Nanoscale* **2019**, *11*, 20261–20273.

(32) Roncato, F.; Rruqa, F.; Porcù, E.; Casarin, E.; Ronca, R.; Maccarinelli, F.; Realdon, N.; Basso, G.; Alon, R.; Viola, G.; Morpurgo, M. Improvement and extension of anti-EGFR targeting in breast cancer therapy by integration with the avidin-nucleic-acid-nano-assemblies. *Nat. Commun.* **2018**, *9*, 4070.

(33) Lu, Y.-J.; Chuang, E.-Y.; Cheng, Y.-H.; Anilkumar, T. S.; Chen, H.-A.; Chen, J.-P. Thermosensitive magnetic liposomes for alternating magnetic field-inducible drug delivery in dual targeted brain tumor chemotherapy. *Chem. Eng. J.* **2019**, *373*, 720–733.

(34) Kutty, R. V.; Chia, S. L.; Setyawati, M. I.; Muthu, M. S.; Feng, S.-S.; Leong, D. T. In vivo and ex vivo proofs of concept that cetuximab conjugated vitamin E TPGS micelles increases efficacy of delivered docetaxel against triple negative breast cancer. *Biomaterials* **2015**, *63*, 58–69.

(35) Mamot, C.; Ritschard, R.; Wicki, A.; Stehle, G.; Dieterle, T.; Bubendorf, L.; Hilker, C.; Deuster, S.; Herrmann, R.; Rochlitz, C. Tolerability, safety, pharmacokinetics, and efficacy of doxorubicin-loaded anti-EGFR immunoliposomes in advanced solid tumours: A phase I dose-escalation study. *Lancet Oncol.* **2012**, *13*, 1234–1241.

(36) Zou, Y.; Meng, F.; Deng, C.; Zhong, Z. Robust, tumor-homing and redox-sensitive polymersomal doxorubicin: A superior alternative to doxil and caelyx? *J. Controlled Release* **2016**, *239*, 149–158.

(37) Fang, Y.; Yang, W.; Cheng, L.; Meng, F.; Zhang, J.; Zhong, Z. EGFR-targeted multifunctional polymersomal doxorubicin induces selective and potent suppression of orthotopic human liver cancer in vivo. *Acta Biomater.* **2017**, *64*, 323–333.

(38) Zhang, Y.; Yue, S.; Haag, R.; Sun, H.; Zhong, Z. An intelligent cell-selective polymersome-DM1 nanotoxin toward triple negative breast cancer. *J. Controlled Release* **2021**, *340*, 331–341.

(39) Zhang, Y.; Wu, K.; Sun, H.; Zhang, J.; Yuan, J.; Zhong, Z. Hyaluronic acid-shelled disulfide-cross-linked nanopolymersomes for ultrahigh-efficiency reactive encapsulation and CD44-targeted delivery of mertansine toxin. *ACS Appl. Mater. Interfaces* **2018**, *10*, 1597–1604.

(40) Yu, N.; Zhang, Y.; Li, J.; Gu, W.; Yue, S.; Li, B.; Meng, F.; Sun, H.; Haag, R.; Yuan, J.; Zhong, Z. Daratumumab Immunopolymersome-Enabled Safe and CD38-Targeted Chemotherapy and Depletion of Multiple Myeloma. *Adv. Mater.* **2021**, *33*, 2007787.

(41) Ding, L.; Gu, W.; Zhang, Y.; Yue, S.; Sun, H.; Cornelissen, J. J. L. M.; Zhong, Z. HER2-specific reduction-sensitive immunopolymerosomes with high loading of epirubicin for targeted treatment of ovarian tumor. *Biomacromolecules* **2019**, *20*, 3855–3863.

(42) Wei, J.; Meng, H.; Guo, B.; Zhong, Z.; Meng, F. Organocatalytic ring-opening copolymerization of trimethylene carbonate and dithiolane trimethylene carbonate: Impact of organocatalysts on copolymerization kinetics and copolymer microstructures. *Biomacromolecules* **2018**, *19*, 2294–2301.

(43) Xiao, X.; Wang, K.; Zong, Q.; Tu, Y.; Dong, Y.; Yuan, Y. Polyprodrug with glutathione depletion and cascade drug activation for multi-drug resistance reversal. *Biomaterials* **2021**, *270*, 120649.

(44) Yi, X.; Hu, J.-J.; Dai, J.; Lou, X.; Zhao, Z.; Xia, F.; Tang, B. Z. Self-guiding polymeric prodrug micelles with two aggregation-induced emission photosensitizers for enhanced chemo-photodynamic therapy. *ACS Nano* **2021**, *15*, 3026–3037.

(45) Tarantino, P.; Carmagnani Pestana, R.; Corti, C.; Modi, S.; Bardia, A.; Tolane, S. M.; Cortes, J.; Soria, J. C.; Curigliano, G. Antibody-drug conjugates: Smart chemotherapy delivery across tumor histologies. *Ca-Cancer J. Clin.* **2021**, DOI: 10.3322/caac.21705.

(46) Walsh, S. J.; Bargh, J. D.; Dannheim, F. M.; Hanby, A. R.; Seki, H.; Counsell, A. J.; Ou, X.; Fowler, E.; Ashman, N.; Takada, Y.; Isidro-

Llobet, A.; Parker, J. S.; Carroll, J. S.; Spring, D. R. Site-selective modification strategies in antibody-drug conjugates. *Chem. Soc. Rev.* **2021**, *50*, 1305–1353.

(47) Amiri-Kordestani, L.; Blumenthal, G. M.; Xu, Q. C.; Zhang, L.; Tang, S. W.; Ha, L.; Weinberg, W. C.; Chi, B.; Candau-Chacon, R.; Hughes, P.; Russell, A. M.; Miksinski, S. P.; Chen, X. H.; McGuinn, W. D.; Palmby, T.; Schrieber, S. J.; Liu, Q.; Wang, J.; Song, P.; Mehrotra, N.; Skarupa, L.; Clouse, K.; Al-Hakim, A.; Sridhara, R.; Ibrahim, A.; Justice, R.; Pazdur, R.; Cortazar, P. FDA approval: Ado-trastuzumab emtansine for the treatment of patients with HER2-positive metastatic breast cancer. *Clin. Cancer Res.* **2014**, *20*, 4436–4441.

(48) Nakai, K.; Hung, M. C.; Yamaguchi, H. A perspective on anti-EGFR therapies targeting triple-negative breast cancer. *Am. J. Cancer Res.* **2016**, *6*, 1609–1623.

(49) Yewale, C.; Baradia, D.; Vhora, I.; Patil, S.; Misra, A. Epidermal growth factor receptor targeting in cancer: A review of trends and strategies. *Biomaterials* **2013**, *34*, 8690–8707.

(50) Karlsen, E.-A.; Kahler, S.; Tefay, J.; Joseph, S. R.; Simpson, F. Epidermal growth factor receptor expression and resistance patterns to targeted therapy in non-small cell lung cancer: A review. *Cells* **2021**, *10*, 1206.

(51) Mohan, N.; Luo, X.; Shen, Y.; Olson, Z.; Agrawal, A.; Endo, Y.; Rotstein, D. S.; Pelosof, L. C.; Wu, W. J. A novel bispecific antibody targeting EGFR and VEGFR2 is effective against triple negative breast cancer via multiple mechanisms of action. *Cancers* **2021**, *13*, 1027.

(52) Xu, W.; Song, C.; Wang, X.; Li, Y.; Bai, X.; Liang, X.; Wu, J.; Liu, J. Downregulation of miR-155-5p enhances the anti-tumor effect of cetuximab on triple-negative breast cancer cells via inducing cell apoptosis and pyroptosis. *Aging* **2021**, *13*, 228–240.

(53) Caratelli, S.; Arriga, R.; Sconocchia, T.; Ottaviani, A.; Lanzilli, G.; Pastore, D.; Cenciarelli, C.; Venditti, A.; Del Principe, M. I.; Lauro, D.; Landoni, E.; Du, H.; Savoldo, B.; Ferrone, S.; Dotti, G.; Sconocchia, G. In vitro elimination of epidermal growth factor receptor-overexpressing cancer cells by CD32A-chimeric receptor T cells in combination with cetuximab or panitumumab. *Int. J. Cancer* **2020**, *146*, 236–247.

(54) Wang, L.; Yao, J.; Shi, X.; Hu, L.; Li, Z.; Song, T.; Huang, C. MicroRNA-302b suppresses cell proliferation by targeting EGFR in human hepatocellular carcinoma SMMC-7721 cells. *BMC Cancer* **2013**, *13*, 448.

(55) Zou, Y.; Xia, Y.; Meng, F.; Zhang, J.; Zhong, Z. GE11-directed functional polymersomal doxorubicin as an advanced alternative to clinical liposomal formulation for ovarian cancer treatment. *Mol. Pharmaceutics* **2018**, *15*, 3664–3671.

(56) Paiva, I.; Mattingly, S.; Wuest, M.; Leier, S.; Vakili, M. R.; Weinfeld, M.; Lavasanifar, A.; Wuest, F. Synthesis and Analysis of <sup>64</sup>Cu-Labeled GE11-Modified Polymeric Micellar Nanoparticles for EGFR-Targeted Molecular Imaging in a Colorectal Cancer Model. *Mol. Pharmaceutics* **2020**, *17*, 1470–1481.

(57) Zhou, C.; Xia, Y.; Wei, Y.; Cheng, L.; Wei, J.; Guo, B.; Meng, F.; Cao, S.; van Hest, J. C. M.; Zhong, Z. GE11 peptide-installed chimaeric polymersomes tailor-made for high-efficiency EGFR-targeted protein therapy of orthotopic hepatocellular carcinoma. *Acta Biomater.* **2020**, *113*, 512–521.

(58) Yin, L.; Qi, X.-W.; Liu, X.-Z.; Yang, Z.-Y.; Cai, R.-L.; Cui, H.-J.; Chen, L.; Yu, S.-C. Icaritin enhances the efficacy of cetuximab against triple-negative breast cancer cells. *Oncol. Lett.* **2020**, *19*, 3950–3958.

(59) Fu, W.; Sun, H.; Zhao, Y.; Chen, M.; Yang, L.; Yang, X.; Jin, W. Targeted delivery of CD44s-siRNA by ScFv overcomes de novo resistance to cetuximab in triple negative breast cancer. *Mol. Immunol.* **2018**, *99*, 124–133.

(60) Humblet, Y. Cetuximab: an IgG1 monoclonal antibody for the treatment of epidermal growth factor receptor-expressing tumours. *Expert Opin. Pharmacother.* **2004**, *5*, 1621–1633.

(61) Tanei, T.; Choi, D. S.; Rodriguez, A. A.; Liang, D. H.; Dobrolecki, L.; Ghosh, M.; Landis, M. D.; Chang, J. C. Antitumor activity of cetuximab in combination with ixabepilone on triple negative breast cancer stem cells. *Breast Cancer Res.* **2016**, *18*, 6.

(62) Oroudjev, E.; Lopus, M.; Wilson, L.; Audette, C.; Provenzano, C.; Erickson, H.; Kovtun, Y.; Chari, R.; Jordan, M. A. Maytansinoid-

antibody conjugates induce mitotic arrest by suppressing microtubule dynamic instability. *Mol. Cancer Ther.* **2010**, *9*, 2700–2713.

(63) Gao, S.; Zhang, W.; Wang, R.; Hopkins, S. P.; Spagnoli, J. C.; Racine, M.; Bai, L.; Li, L.; Jiang, W.; Yang, X.; Lee, C.; Nagata, K.; Howerth, E. W.; Handa, H.; Xie, J.; Ma, Q.; Kumar, A. Nanoparticles encapsulating nitrosylated maytansine to enhance radiation therapy. *ACS Nano* **2020**, *14*, 1468–1481.

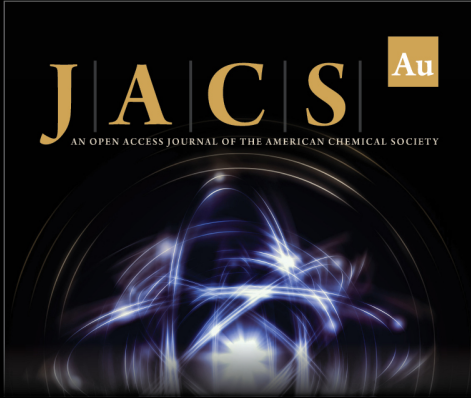
(64) Adams, S. R.; Yang, H. C.; Savariar, E. N.; Aguilera, J.; Crisp, J. L.; Jones, K. A.; Whitney, M. A.; Lippman, S. M.; Cohen, E. E. W.; Tsien, R. Y.; Advani, S. J. Anti-tubulin drugs conjugated to anti-ErbB antibodies selectively radiosensitize. *Nat. Commun.* **2016**, *7*, 13019.

(65) Chen, L.; Zhang, T.; Sun, S.; Ren, W.; Wu, A.; Xu, H. Ultrasound-mediated cavitation enhances EGFR-targeting PLGA-PEG nanomicelle delivery for triple-negative breast cancer treatment. *Cancers* **2021**, *13*, 3383.

(66) Meng, H.; Zou, Y.; Zhong, P.; Meng, F.; Zhang, J.; Cheng, R.; Zhong, Z. A smart nano-prodrug platform with reactive drug loading, superb stability, and fast responsive drug release for targeted cancer therapy. *Macromol. Biosci.* **2017**, *17*, 1600518.

(67) Zhong, P.; Gu, X.; Cheng, R.; Deng, C.; Meng, F.; Zhong, Z.  $\alpha\text{v}\beta\text{3}$  integrin-targeted micellar mertansine prodrug effectively inhibits triple-negative breast cancer in vivo. *Int. J. Nanomed.* **2017**, *12*, 7913–7921.

(68) Zhong, P.; Zhang, J.; Deng, C.; Cheng, R.; Meng, F.; Zhong, Z. Glutathione-sensitive hyaluronic acid-ss-mertansine prodrug with a high drug content: Facile synthesis and targeted breast tumor therapy. *Biomacromolecules* **2016**, *17*, 3602–3608.



**JACS** Au  
AN OPEN ACCESS JOURNAL OF THE AMERICAN CHEMICAL SOCIETY

Editor-in-Chief  
**Prof. Christopher W. Jones**  
Georgia Institute of Technology, USA

**Open for Submissions** 

pubs.acs.org/jacsau  ACS Publications  
Most Trusted. Most Cited. Most Read.